High-resolution magneto-optical spectroscopy of $^{7}LiYF_4$:$^{167}Er^{3+}$, $^{166}Er^{3+}$ and analysis of hyperfine structure of ultranarrow optical transitions

K. I. Gerasimov,[1,*] M. M. Minnegaliev,[1] B. Z. Malkin,[2] E. I. Baibekov,[1,2] and S. A. Moiseev[1]

[1]*Kazan Quantum Center, Kazan National Research Technical University, 10 K. Marx Street, Kazan 420111, Russia*

[2]*Kazan (Volga Region) Federal University, 18 Kremlyovskaya Street, Kazan 420008, Russia*

(Received 5 June 2016; published 29 August 2016)

We performed high-resolution magneto-optical spectroscopy of the hyperfine transitions from $^{4}I_{15/2}$ to the $^{4}I_{13/2}$ and $^{4}I_{9/2}$ multiplets of $^{167}Er^{3+}$ and $^{166}Er^{3+}$ in an isotopically purified $^{7}LiYF_4$ crystal in various external magnetic fields up to 0.7 T. The obtained experimental results are interpreted in the framework of the generalized theoretical approach. The derived model successfully explains all the experimentally observed optical hyperfine transitions by using a single set of basic parameters found for the crystal-field interaction, magnetic dipole and electric quadrupole hyperfine interactions, together with Zeeman interactions at different orientations of the external magnetic field. A number of the studied quantum transitions appears to be promising for use in Raman quantum storage at optical telecommunication wavelengths.

DOI: 10.1103/PhysRevB.94.054429

I. INTRODUCTION

Dielectric crystals doped with rare-earth ions are promising materials that can be used for the implementation of solid state multiqubit quantum memory (QM) cells [1–5] (see also the special issues of the journals [6,7]). In a series of rare-earth ions, special interest has been shown for a trivalent erbium ion having wavelengths of the quantum transitions in the transparency windows of optical fiber communications, which makes this ion the most promising choice for the creation of quantum repeaters operating in the first and third low-loss windows of optical fibers (0.8–0.9 and 1.55 μm, respectively) [8–11]. Moreover, a high-quality $LiYF_4$ single crystal doped with rare-earth ions can be grown in the form of an optical fiber [12] that should facilitate the integration of quantum repeaters in optical networks. It is well known that the inhomogeneous linewidths of optical transitions can be small enough, and the hyperfine structure can be fully or partially resolved for rare-earth (RE) ions in dielectric crystals [13,14]. In these tasks high-resolution magneto-optical spectroscopy is a very powerful technique in establishing the basic information about the wave functions and quantum transitions between hyperfine sublevels of the ground and excited multiplets [15–17].

Recently, it has been found that $^{170}Er^{3+}$ ions have very narrow linewidths [full width at half maximum (FWHM) of 16 MHz] of $^{4}I_{15/2} \rightarrow {}^{4}I_{13/2}$ optical transitions in an isotopically enriched $^{7}LiYF_4$ crystal [18]. In turn, the presence of an ultranarrow absorption line opens a principle possibility for the implementation of QM protocols based on off-resonant Raman echo schemes [19–22]. This approach provides direct storage of multimode light pulses on long-lived hyperfine sublevels and promises the highest quantum efficiency [23]. Also, we note that a 6-h coherence time of electron-nuclear states has been demonstrated by using a frozen core effect and zero first-order Zeeman shift method, accompanied by the dynamical decoupling technique [24] of rare-earth ions in an inorganic crystal, which gives a serious consideration for the implementation of QM devices in these materials.

Erbium has one odd-number isotope, $^{167}Er^{3+}$, with a natural abundance of 22.9% and nuclear spin $I = 7/2$. The rich structure of the hyperfine levels of this isotope can be used for long-lived QM based on off-resonant Raman echo schemes. In order to find the optimal Λ scheme of optical transitions and to prepare the appropriate initial quantum state of ions in these types of experiments, one has to know the crystal-field wave functions and the hyperfine structure of the optical transitions.

The crystal-field splittings of the energy levels of impurity Er^{3+} ions in $LiYF_4$ have been extensively studied earlier [25–32]. The hyperfine parameters of the ground state are known from electron paramagnetic resonance (EPR) spectroscopy data [33]. Detailed experimental and theoretical studies of the crystal-field levels, including the analysis of hyperfine interactions, have been implemented for infrared transitions $^{4}I_{15/2} \rightarrow {}^{4}I_{13/2}, {}^{4}I_{11/2}$ in Er^{3+} ions, and more accurate crystal-field parameters have been also obtained [34,35]. The hyperfine structure of the $^{4}I_{15/2} \rightarrow {}^{4}F_{9/2}$ transition of Er^{3+} ions has been investigated even earlier [36] in the isotopically pure crystal $^{7}LiYF_4$.

Caused by the increasing interest in this crystal for optical quantum storage, additional investigations of the energy level structure and coherence lifetimes in the external magnetic fields have been recently performed for the $^{4}I_{15/2} \rightarrow {}^{4}I_{13/2}$ transition [37]. Crystals with a natural abundance of Er and Li ions were used in Ref. [37], which highly complicated the spectroscopic investigation due to isotopic broadening of the resonant transitions. Herein, hole burning spectroscopy was used to obtain the zero magnetic field hyperfine structure of the lowest level of the $^{4}I_{13/2}$ excited state and to measure the longitudinal relaxation time of two hyperfine sublevels of the ground state. The high-resolution absorption spectrum at zero magnetic field confirmed the previous results [35]. However, the optical transitions between hyperfine levels at the magnetic field (2.2 T) were not spectroscopically resolved due to high magnetic field inhomogeneity, and the properties of hyperfine transitions in the external magnetic fields were not experimentally investigated, respectively. Moreover, information about the hyperfine structure of the $^{4}I_{15/2} \rightarrow {}^{4}I_{9/2}$ transitions lying in the first fiber transparency window is absent. It is worth

*kigerasimov@mail.ru

noting that the existing theoretical models do not provide a general analysis of the hyperfine interactions including intermultiplet mixing, which could affect the frequencies and intensities of the optical transitions.

In this paper, we have performed high-resolution magneto-optical spectroscopy studies of the hyperfine structure of several transitions from $^4I_{15/2}$ to the $^4I_{13/2}$ and $^4I_{9/2}$ multiplets of $^{167}Er^{3+}$ and $^{166}Er^{3+}$ in an isotopically purified $^7LiYF_4$ crystal in external magnetic fields up to 0.7 T. The obtained results of our measurements are successfully interpreted in the framework of the generalized theoretical approach taking into account the crystal-field interaction, both magnetic dipole and electric quadrupole hyperfine interactions, and also Zeeman interactions at several orientations of the external magnetic field. A single set of basic parameters of the noted interactions has been determined from an analysis of the experimental data. Herein, a number of the observed transitions appear to be promising for use in Raman quantum storage at telecommunication wavelengths due to their rather narrow linewidths.

II. EXPERIMENTAL PROCEDURE

Single crystals $^7LiYF_4$:$^{166}Er^{3+}$ (0.005 at. %) and $^7LiYF_4$:$^{167}Er^{3+}$ (0.005 at. %) have been grown by the Bridgman-Stockbarger method. The starting melt for ^7Li was $^7LiOH \cdot H_2O$ with 99.95% purity of ^7Li. This compound was transferred to the ^7LiF in a chemical reaction with NH_4HF_2 at a temperature of 350°C. The starting materials of the admixtures were $^{166}Er_2O_3$ and $^{167}Er_2O_3$ with the purity of the erbium isotopes of 98% and 96%, respectively. Finally, the starting materials were high-purity (99.99%) YF_3, ^7LiF, and $^{166}Er_2O_3$ or $^{167}Er_2O_3$. Lithium fluoride (52 mol %) and yttrium fluoride (48 mol %) were preliminarily melted together in a fluorinating atmosphere and then kept for 20–24 h at a temperature slightly below the melting point to pass the solid-state synthesis preparation phase. After adding $^{166}Er_2O_3$ or $^{167}Er_2O_3$, the obtained compound was used for the final growth stage. Crystal growth was accomplished at 820 °C with a pulling rate of 1 mm/h.

High-resolution transmission spectra were measured by using single-frequency tunable lasers. A Tekhnoscan TIS-SF-777 Ti:sapphire laser with a linewidth of 5 kHz over 1 s and a New Focus TLB-6728 diode laser with a linewidth of 200 kHz over 50 ms were used for investigations of the $^4I_{15/2} \rightarrow {}^4I_{9/2}$ and $^4I_{15/2} \rightarrow {}^4I_{13/2}$ transitions, respectively. A Montana Instruments helium-free optical cryostat system with a magneto-optic module was used for cooling the samples to the temperature of ∼4 K. The magnetic field was perpendicular or parallel to the crystal c axis and could be set between −0.7 and 0.7 T. An external Fabry-Pérot cavity with a free spectral range of 354.4 MHz was used to control and to correct the nonlinear frequency scanning of the lasers. Different parts of the absorption spectra were calibrated with a relative accuracy of 3–4 MHz. The transition frequency was determined by a wave meter with an absolute accuracy of 2–3 GHz. $^4I_{15/2} \rightarrow {}^4I_{9/2}$ and $^4I_{15/2} \rightarrow {}^4I_{13/2}$ transitions occur near the vacuum wavelengths of 809.01 and 1530.42 nm, respectively. Thorlabs avalanche photodiodes APD120A/M and APD110S/M were used for optical detection in the corresponding spectral ranges.

TABLE I. The lowest-state g factors of three studied multiplets of $^7LiYF_4$:$^{166}Er^{3+}$ and the linewidths of the transitions from the ground state (in MHz) for σ- and π-polarized light. Calculated g factors are given in square brackets.

				Linewidth	
Multiplet	Γ	$g_\perp$	$g_\parallel$	σ	π
$^4I_{9/2}$	Γ_{78}	2.94(2) [3.07]	3.72(2) [3.71]	160	130
$^4I_{13/2}$	Γ_{56}	5.94(5) [5.91]	1.30(2) [1.59]	160	110
	Γ_{78}	7.32(5) [7.35]	1.52(2) [1.53]	70	50
$^4I_{15/2}$	Γ_{56}	8.10(2) [8.17]	3.13(2) [3.11]		
		8.105[a]	3.137[a]		

[a]Reference [33].

Conventional techniques of light amplitude modulation and lock-in detection were used to increase the signal-to-noise ratio in the measured spectra.

III. EXPERIMENTAL RESULTS

The energy levels of the ground electronic $4f^{11}$ configuration of Er^{3+} ions which substitute for Y^{3+} ions are characterized by the irreducible representations (irreps) Γ_{56} and Γ_{78} of the S_4 point symmetry group. In this work, optical transitions from the ground state (the lowest doublet Γ_{56} of the $^4I_{15/2}$ multiplet) to two lower sublevels Γ_{78} and Γ_{56} of the $^4I_{13/2}$ multiplet and the lowest sublevel Γ_{56} of the $^4I_{9/2}$ multiplet were investigated for two isotopes of erbium. Trivalent ions of an even ^{166}Er isotope have simple magneto-optical spectra, and the sample doped with the ^{166}Er was used to measure the g factors of the excited states and to estimate the linewidths of the optical transitions. Experimental and theoretical values of the g factors are presented in Table I.

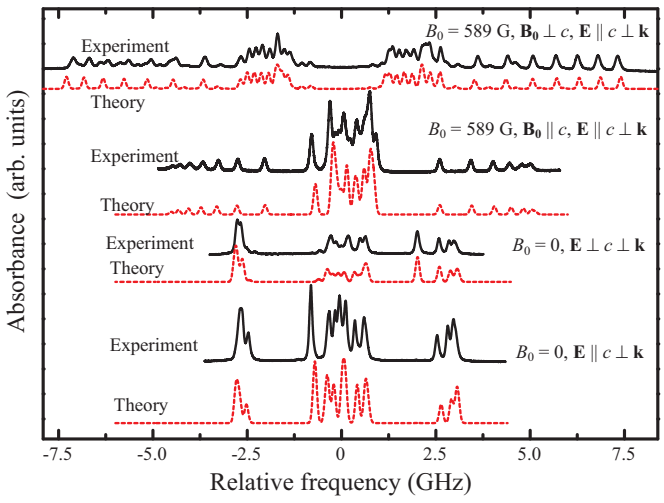

FIG. 1. $^7LiYF_4$:$^{167}Er^{3+}$ (0.005 at. %) single-crystal absorption spectra corresponding to the $^4I_{15/2}(\Gamma_{56}) \rightarrow {}^4I_{9/2}(\Gamma_{78})$ transition at $B_0 = 0$ and $B_0 = 589$ G and two orientations of the crystal sample. Experimental data and the results of calculations are represented by solid black and red dotted lines, respectively. Frequency origin at $B_0 = 0$ corresponds to 370.574 THz transition. $T = 4$ K, c is the crystal's C_4 axis, $\mathbf{E}$ and $\mathbf{k}$ denote the electric field and the wave vector of the incident radiation, respectively.

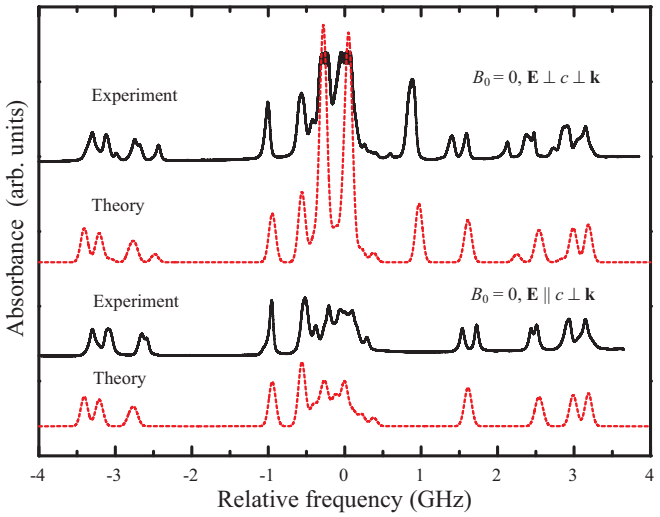

FIG. 2. $^{7}LiYF_4$:$^{167}Er^{3+}$ (0.005 at. %) single-crystal absorption spectra corresponding to the $^4I_{15/2}(\Gamma_{56}) \rightarrow {}^4I_{13/2}(\Gamma_{56})$ transition at $B_0 = 0$ and two orientations of the crystal sample. Experimental data and the simulated spectra are represented by solid black and red dotted lines, respectively. Frequency origin at $B_0 = 0$ corresponds to 196.013 THz transition. $T = 4$ K.

The ground-state g factors are in good agreement with the ones measured by EPR [33]. The absorption linewidths of the $^{166}Er^{3+}$ isotope measured for three optical transitions are also shown in Table I.

The optical transmission spectra of the $^{167}Er^{3+}$ ion (nuclear spin $I = 7/2$) have a richer structure in comparison with even isotopes due to the hyperfine splitting of each Kramers state into nine sublevels (two singlets, four doublets, and three quasidoublets). The external magnetic field B_0 removes the residual degeneracy of the hyperfine levels. The absorption spectrum becomes especially complex at low magnetic fields, when the Zeeman and hyperfine interactions are comparable to each other. Zero- and low-field experimental spectra corresponding to the $^4I_{15/2}(\Gamma_{56}) \rightarrow {}^4I_{9/2}(\Gamma_{78})$ transition and their theoretical simulations for the two sample orientations are shown in Fig. 1.

We have observed the linewidths ~90 MHz for the $^4I_{15/2}(\Gamma_{56}) \rightarrow {}^4I_{9/2}(\Gamma_{78})$ transition with the highest optical line density ~0.8 cm^{-1} that seems very promising for the implementation of the off-resonant Raman Λ scheme.

The observed absorption lines of $^4I_{15/2}(\Gamma_{56}) \rightarrow {}^4I_{13/2}(\Gamma_{56})$, $^4I_{13/2}(\Gamma_{78})$ optical transitions are more narrow and intensive (see Figs. 2–4). However, spatial inhomogeneity of the magnetic field of ~0.1–0.2 G/mm (at $B_0 = 500$ G) resulted in a visible broadening of the sideband lines at $B_0 > 500$ G (see Fig. 3). The measured linewidths were ~35 and ~55 MHz at $B_0 = 0$, and the highest optical densities of the hyperfine transitions were ~2 and ~1.5 cm^{-1}, respectively. These results are very close to the record linewidth (16 MHz) reported in Ref. [18] for an even (170) isotope of erbium, which indicates a comparable quality of the studied crystals.

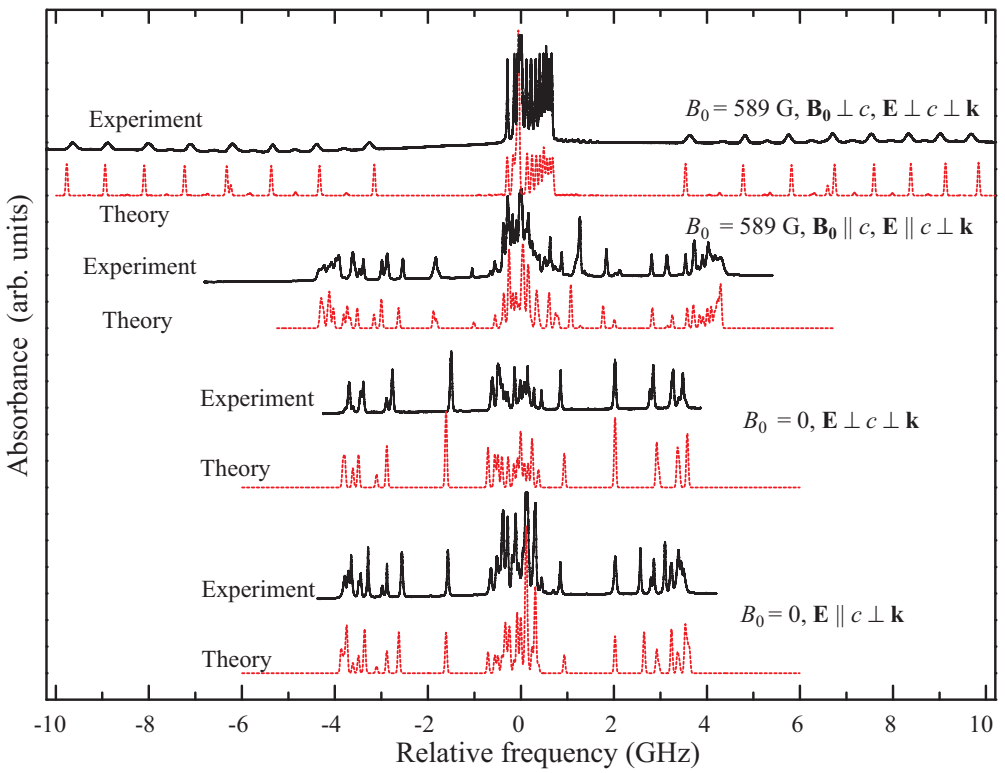

FIG. 3. $^{7}LiYF_4$:$^{167}Er^{3+}$ (0.005 at. %) single-crystal absorption spectra corresponding to the $^4I_{15/2}(\Gamma_{56}) \rightarrow {}^4I_{13/2}(\Gamma_{78})$ transition at $B_0 = 0$ and $B_0 = 589$ G and two orientations of the crystal sample. Experimental data and the results of calculations are represented by solid black and red dotted lines, respectively. Frequency origin at $B_0 = 0$ corresponds to 195.893 THz transition. $T = 4$ K.

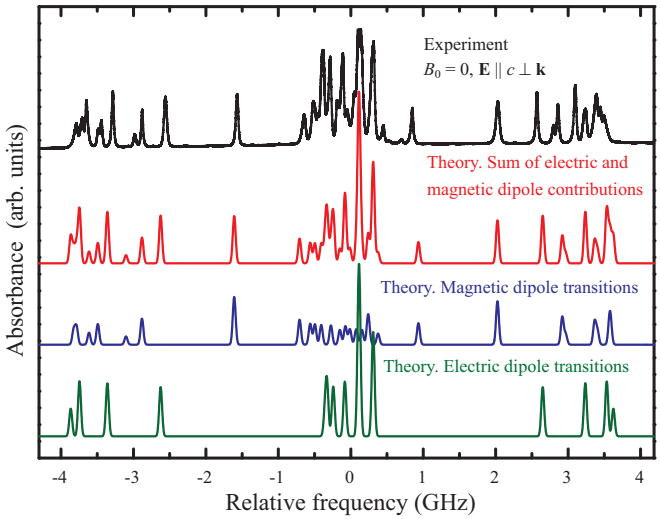

FIG. 4. Demonstration of the mixed nature of the ${}^4I_{15/2}(\Gamma_{56}) \rightarrow {}^4I_{13/2}(\Gamma_{78})$ transition. The upper (black) and the second (red) curves represent the experimental and calculated ${}^7LiYF_4$:${}^{167}Er^{3+}$ (0.005 at. %) single-crystal absorption spectra at $B_0 = 0$ and $T = 4$ K. The two bottom (blue and green) curves are the calculated contributions of the magnetic and electric dipole transitions, respectively.

IV. THEORY AND DISCUSSION

We follow essentially the calculation procedure described in previous publications [35,38]. In order to simulate the absorption spectra, we considered the following Hamiltonian of the ${}^{167}Er^{3+}$ ion,

$$H = H_{\rm FI} + H_{\rm CF} + H_{\rm Z} + H_{\rm HF}, \tag{1}$$

where $H_{\rm FI}$ is the free-ion standard Hamiltonian [39] that operates on the basis of 364 states of the electronic $4f^{11}$ configuration, $H_{\rm CF} = \sum_{pk} B_p^k O_p^k$ is the crystal-field Hamiltonian (O_p^k are linear combinations of spherical tensor operators defined in Ref. [40]), $H_{\rm Z} = -\boldsymbol{\mu}\mathbf{B}_0$ is the Zeeman interaction, $\boldsymbol{\mu} = -\mu_{\rm B}(\mathbf{L} + 2\mathbf{S})$ is the magnetic moment of the Er^{3+} ion ($\mathbf{L}$ and $\mathbf{S}$ are the orbital and spin moments of the $4f$ shell, respectively, and μ_B is the Bohr magneton), and $H_{\rm HF}$ is the hyperfine interaction. Parameters of the free-ion Hamiltonian used in the calculations are presented in Table II. The crystal-field parameters B_4^4 and B_4^{-4} were slightly corrected with respect to Ref. [41] in order to obtain the best fit of the ground and the excited-state electronic g factors (see Tables I and III).

The 364 electronic eigenstates of the Hamiltonian (1) were found by numerical diagonalization of the operator $H_0 = H_{\rm FI} + H_{\rm CF} + H_{\rm Z}$. The lower parts of these eigenstates corresponding to the energy band of 0–13 000 $\rm cm^{-1}$ were used

TABLE II. Parameters of the free-ion Hamiltonian (standard notation; see Ref. [42]), $\rm cm^{-1}$.

F^2	F^4	F^6	ζ	α	β	γ	
96329	68001	54342	2370	17.79	1800	−582.1	
T^2	T^3	T^4	T^6	T^7	T^8	M^0	P^2
451	61	100	−245	305	160	3.86	594

TABLE III. The crystal-field parameters in $\rm cm^{-1}$.

p	k	B_p^k (present work)	B_p^k [41]
2	0	190	190
4	0	−80	−80
4	4	−760.8	−771
4	−4	−679.4	−667
6	0	−2.3	−2.3
6	4	−363	−363
6	−4	−222	−222

to form a truncated space of 52 states. The total Hamiltonian (1) was projected on this truncated space of electronic wave functions and then diagonalized numerically within the basis of $52 \times 8 = 416$ electron-nuclear states taking into account the magnetic ($H_{\rm HFM}$) and electric quadrupole ($H_{\rm HFQ}$) interactions in $H_{\rm HF}$:

$$\begin{aligned} H_{\rm HFM} = \mu_{\rm B}\gamma_{\rm N}\hbar\left\langle\frac{1}{r^3}\right\rangle_{4f}\sum\big\{&2Il + O_2^0(3s_zI_z - sI) \\ &+ 3O_2^2(s_xI_x - s_yI_y) + 3O_2^{-2}(s_xI_y + s_yI_x) \\ &+ 6O_2^1(s_xI_z + s_zI_x) + 6O_2^{-1}(s_zI_y + s_yI_z)\big\}, \end{aligned} \tag{2}$$

$$\begin{aligned} H_{\rm HFQ} = &\frac{e^2Q(1-\gamma_\infty)}{4I(2I-1)}\sum_L q_L\frac{3z_L^2 - r_L^2}{r_L^5}I_0 \\ &- \frac{e^2Q(1-R_Q)}{4I(2I-1)}\left\langle\frac{1}{r^3}\right\rangle_{4f}\sum\big[O_2^0I_0 + 3O_2^2I_2 \\ &+ 3O_2^{-2}I_{-2} + 6O_2^1I_1 + 6O_2^{-1}I_{-1}\big]. \end{aligned} \tag{3}$$

Above, the sums are taken over $4f$ electrons, e is the elementary charge, l and s are the one-electron orbital and spin moments, respectively, $\gamma_{\rm N}/2\pi = -1.23$ MHz/T is the gyromagnetic ratio, $Q = 2.83 \times 10^{28}$ $\rm m^2$ is the quadrupole moment of the ${}^{167}Er$ nucleus, and γ_∞ and R_Q are Sternheimer antishielding and shielding factors [43]. The expectation value of the $1/r^3$ operator of the $4f$ electrons, $\langle 1/r^3\rangle_{4f}$, equals 11.07 atomic units (a.u.) [44]. The first term in Eq. (3) comes from the crystal lattice contribution to the electric field gradient at the nucleus and contains the sum over the host lattice ions with charges eq_L and radius vectors $\mathbf{r}_L$ relative to the considered erbium ion. The second term is the contribution of the $4f$ electrons, where the following nuclear spin operators were used: $I_0 = 3I_z^2 - I(I+1)$, $I_2 = I_x^2 - I_y^2$, $I_{-2} = I_xI_y + I_yI_x$, $I_1 = I_xI_z + I_zI_x$, $I_{-1} = I_zI_y + I_yI_z$. As expected, the contribution of $H_{\rm HFQ}$ into the line splittings was rather small, ∼5% with respect to $H_{\rm HFM}$.

The absorption probability was determined by the electric dipole and magnetic dipole line strengths, which, for a given hyperfine transition $|i\rangle \rightarrow |f\rangle$, equal

$$S_{if,q}^{\rm (ED)} = |\langle i|d_q|f\rangle|^2, \quad S_{if,q'}^{\rm (MD)} = |\langle i|\mu_{q'}|f\rangle|^2, \tag{4}$$

where q and q' denote the polarization of the electric and magnetic field, respectively, the magnetic moment operator $\boldsymbol{\mu}$ is defined above, and $\mathbf{d}$ is the effective electric dipole moment

TABLE IV. The dipolar coupling parameters b_p^k, in units of $10^{-4}e$ nm.

p	k	b_p^k	p	k	b_p^k
2	1	6.2	6	1	2.7
2	−1	−7.7	6	−1	−6.2
2	2	1.20	6	2	−2.0
2	−2	−0.12	6	−2	13.1
4	1	−8.5	6	3	−6.5
4	−1	18.1	6	−3	18.9
4	2	3.12	6	5	−28.8
4	−2	0.51	6	−5	4.6
4	3	−20.8	6	6	−1.35
4	−3	−25.6	6	−6	−0.08

with components

$$\begin{aligned} d_x &= b_2^1 O_2^1 + b_2^{-1} O_2^{-1} + b_4^1 O_4^1 + b_4^{-1} O_4^{-1} \\ &\quad + b_4^3 O_4^3 + b_4^{-3} O_4^{-3} + b_6^1 O_6^1 + b_6^{-1} O_6^{-1} \\ &\quad + b_6^3 O_6^3 + b_6^{-3} O_6^{-3} + b_6^5 O_6^5 + b_6^{-5} O_6^{-5}, \\ d_y &= b_2^{-1} O_2^1 - b_2^1 O_2^{-1} + b_4^{-1} O_4^1 - b_4^1 O_4^{-1} \\ &\quad - b_4^{-3} O_4^3 + b_4^3 O_4^{-3} + b_6^{-1} O_6^1 - b_6^1 O_6^{-1} \\ &\quad - b_6^{-3} O_6^3 + b_6^3 O_6^{-3} + b_6^{-5} O_6^5 - b_6^5 O_6^{-5}, \\ d_z &= b_2^2 O_2^2 + b_2^{-2} O_2^{-2} + b_4^2 O_4^2 + b_4^{-2} O_4^{-2} \\ &\quad + b_6^2 O_6^2 + b_6^{-2} O_6^{-2} + b_6^6 O_6^6 + b_6^{-6} O_6^{-6}. \end{aligned} \tag{5}$$

The dipolar coupling parameters b_p^k were calculated previously assuming the $4f \leftrightarrow 5d$ configuration mixing [35], and corrected in the present work in order to fit the observed relative intensities of different $|i\rangle \rightarrow |f\rangle$ transitions (see Table IV).

To reproduce the measured spectra, the absorption intensities were calculated assuming a Gaussian line shape of each $|i\rangle \rightarrow |f\rangle$ transition $g(\Delta) = \frac{1}{\sqrt{2\pi\sigma^2}} \exp(-\Delta^2/2\sigma^2)$ with a chosen standard deviation σ:

$$f(\omega) = \sum_{if} \left(\chi^{(\mathrm{ED})} S_{if,q}^{(\mathrm{ED})} + \chi^{(\mathrm{MD})} S_{if,q'}^{(\mathrm{MD})} \right) g(\omega - \omega_{if}). \tag{6}$$

The sums over i and f were taken over all states of the ground and excited electronic doublets, giving $16 \times 16 = 256$ possible hyperfine transitions, though not all of them were allowed by the selection rules. The factors $\chi^{(\mathrm{ED})} = (n^2 + 2)^2/9n = 1.29$ and $\chi^{(\mathrm{MD})} = n = 1.45$ contain the refractive index corrections (here $n = 1.45$ is the refractive index of the $LiYF_4$ crystal [45]). Actually, $\chi^{(\mathrm{ED})}$ lies somewhere within the bounds $0.69 \leqslant \chi \leqslant 1.29$, depending on whether or not the local field correction $\chi_{\mathrm{loc}} = (n^2 + 2)^2/9$ is taken into account (see Ref. [16], Chap. 2). Our calculations with the plausible values of b_p^k listed in Table IV gave the best agreement with the experimental data when using $\chi^{(\mathrm{ED})} = 0.90$.

Group-theoretical analysis allows us to classify the studied hyperfine transitions. The irreps Γ_{56} and Γ_{78} of the S_4 point symmetry group that characterize the electronic Kramers states are related to even and odd irreps of the full rotation group: $D_{1/2}^+ = \Gamma_{56}$, $D_{1/2}^- = \Gamma_{78}$ [46]. The states of the ^{167}Er nucleus ($I = 7/2$) transform according to the $D_{7/2}^+$ representation.

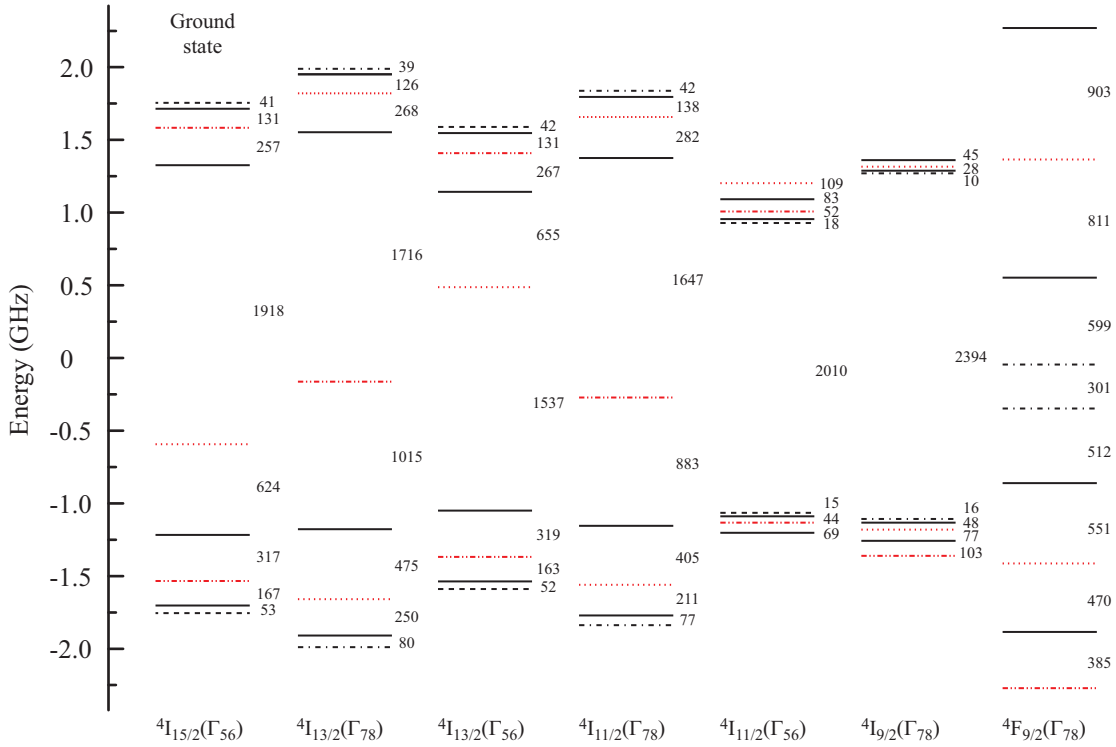

FIG. 5. The calculated hyperfine structure schemes of Kramers levels of $^{167}Er^{3+}$ in $^7LiYF_4$ involved in narrow optical transitions. $B_0 = 0$. Singlet hyperfine levels Γ_1 and Γ_2 are represented by dashed and dashed-dotted black lines, respectively. Doublet hyperfine levels Γ_{34} are represented by solid black lines. Quasidoublet levels Γ_1,Γ_1 and Γ_2,Γ_2 are marked by dotted and dashed-dotted-dotted red lines, respectively. Energy distances between the levels are shown in MHz.

TABLE V. The selection rules showing the allowed electric and magnetic dipole transitions between different hyperfine states characterized by the irreps Γ_1, Γ_2, and Γ_{34}.

Polarization		Allowed transitions
π	$\mathbf{E}\parallel c$	$\Gamma_1 \leftrightarrow \Gamma_2, \Gamma_{34} \rightarrow \Gamma_{34}$
	$\mathbf{B}\perp c$	$\Gamma_1 \leftrightarrow \Gamma_{34}, \Gamma_2 \leftrightarrow \Gamma_{34}$
σ	$\mathbf{E}\perp c$	$\Gamma_1 \leftrightarrow \Gamma_{34}, \Gamma_2 \leftrightarrow \Gamma_{34}$
	$\mathbf{B}\parallel c$	$\Gamma_1 \rightarrow \Gamma_1, \Gamma_2 \rightarrow \Gamma_2, \Gamma_{34} \rightarrow \Gamma_{34}$

Thus, 16 hyperfine wave functions are characterized by the product $D^{\pm}_{1/2} \times D^{+}_{7/2} = D^{\pm}_{3} + D^{\pm}_{4}$. The latter are expanded into the irreps of S_4 group as

$$D^{+}_{3} = \Gamma_1 + 2\Gamma_2 + 2\Gamma_{34}, \quad D^{+}_{4} = 3\Gamma_1 + 2\Gamma_2 + 2\Gamma_{34},$$
$$D^{-}_{3} = 2\Gamma_1 + \Gamma_2 + 2\Gamma_{34}, \quad D^{-}_{4} = 2\Gamma_1 + 3\Gamma_2 + 2\Gamma_{34}, \tag{7}$$

which correspond to eight singlets Γ_1,Γ_2 and four doublets Γ_{34}, and constitute two bands of seven and nine states. As shown by our numerical calculations of the energy spectra, six singlet states actually form three quasidegenerate pairs with the splittings inside each pair $\leqslant$6 MHz (usually $<$1 MHz). Experimentally, the two levels (Γ_1,Γ_1) or (Γ_2,Γ_2) of these quasidoublets are unresolved. The calculated hyperfine structure schemes of several Kramers levels are shown in Fig. 5.

The selection rules governing the electric and magnetic dipole transitions are presented in Table V. As seen in Figs. 1–3, our calculations of absorption spectra are in good agreement with the experimental data. Frequencies and intensities of the observed absorption lines for all studied transitions, at different orientations of the crystal sample and in the range of $B_0 = 0$–1500 G, were simulated correctly using a single set of parameters, most of which had been determined independently in previous studies. The remaining discrepancies (e.g., the observed two close lines at $\sim$1.5 GHz in Fig. 2 instead of a single line) possibly originate from the lattice deformations and/or structure defects which lower the tetragonal symmetry of the studied crystal sample. Using our theoretical approach, we were able to match all the $^4I_{15/2}(\Gamma_{56}) \rightarrow {}^4I_{9/2}(\Gamma_{78})$, $^4I_{13/2}(\Gamma_{78})$, $^4I_{13/2}(\Gamma_{56})$ absorption lines with particular hyperfine transitions (see the tables of squared matrix elements and of the transition frequencies in the Supplemental Material [47]).

Our calculations confirm that $^4I_{15/2}(\Gamma_{56}) \rightarrow {}^4I_{9/2}(\Gamma_{78})$ transition is an electric dipole one. At $B_0 = 0$, the absorption spectrum consists of 17 and 28 partially degenerate hyperfine transitions with nonzero intensities for π ($\mathbf{E}\parallel c\perp\mathbf{k}$) and σ ($\mathbf{E}\perp c\perp\mathbf{k}$) polarization of the light beam, respectively. The Zeeman interaction lifts the degeneracy and mixes different hyperfine states. At $B_0 = 589$ G, we discern about 30 and 56 transitions at $\mathbf{B}_0\parallel c$, or about 120 and 93 transitions at $\mathbf{B}_0\perp c$, for π and σ polarization, respectively.

Spectra of the $^4I_{15/2} \rightarrow {}^4I_{13/2}$ transitions are even more complex because they contain both electric and magnetic dipole contributions. Our experimental scheme and the use of isotopically purified ^{167}Er made it possible to resolve the hyperfine structure and pick out the electric and magnetic dipole transitions (see Fig. 4). Already at zero magnetic field, the absorption spectra consist of 45 and 28 hyperfine transitions for π and σ polarization, respectively. According to our calculations, magnetic dipole transitions contribute to $\sim$20% of the overall $^4I_{15/2} \rightarrow {}^4I_{13/2}$ absorption intensity.

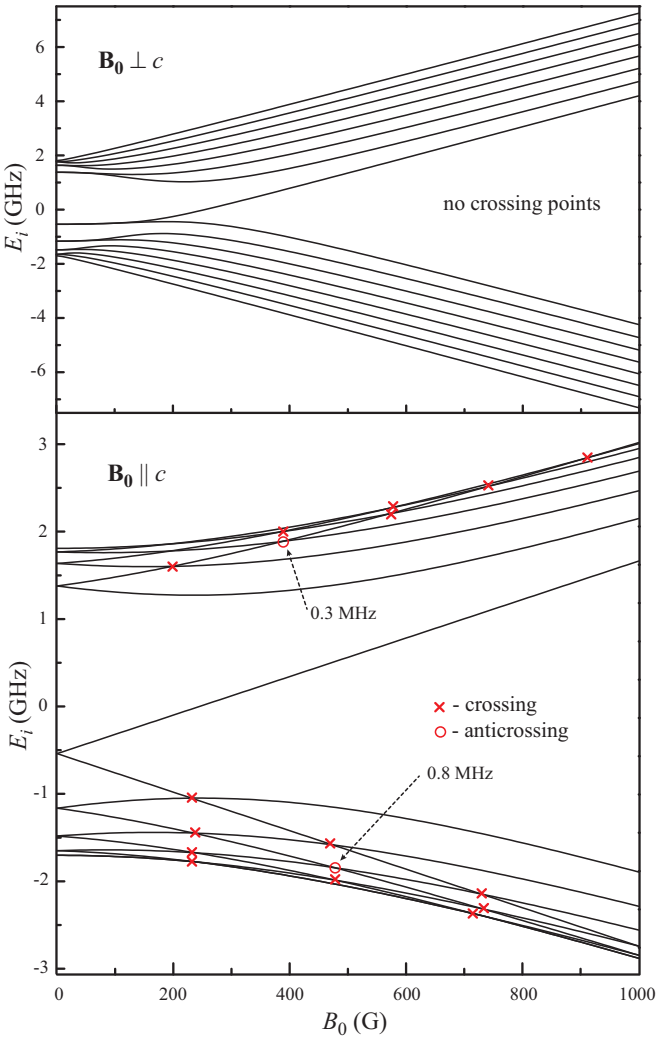

FIG. 6. Calculated energies of the ground-state hyperfine levels vs magnetic field. Crossing and anticrossing points with gaps of 0.3 and 0.8 MHz are shown as red crosses and circles, respectively.

Reasonable agreement of the simulated spectra with the experimental data for all three studied transitions substantiates the calculated wave functions of the hyperfine sublevels. This knowledge opens the way for the construction of effective Λ schemes for optical Raman QM protocols. For this purpose, it is natural to choose the lower Kramers states of the ground and optically excited multiplets, since, due to longer nonradiative lifetimes, they provide narrower absorption lines. Some of the calculated hyperfine structure schemes of Er^{3+} in $LiYF_4$ involved in narrow transition lines are shown in Fig. 5.

The eigenenergies and the wave functions depend on the external magnetic field in a rather complex manner. The calculated dependencies of the ground-state energies on B_0 are presented in Fig. 6. At $B_0 < 500$ G, when hyperfine and Zeeman interactions are competing with each other, the dependencies are nonlinear in B_0. These calculations can be

used as a starting point for the zero first-order Zeeman shift method, i.e., in the search for the conditions (strength and orientation of the magnetic field) when the transition frequency weakly depends on B_0. The latter is expected to reduce the magnetic contributions to the homogeneous linewidth [48]. However, considering the complexity of the studied level schemes, a search of these conditions is beyond the scope of the present work.

V. CONCLUSION

In this work, we have observed and theoretically described a well-resolved hyperfine structure of three optical transitions of $^{167}Er^{3+}$ and $^{166}Er^{3+}$ in isotopically purified $^{7}LiYF_4$ crystals. High-resolution absorption spectra were measured for two orientations of the crystals in various external magnetic fields up to 0.7 T. Experimental spectroscopic information including the intensities of the hyperfine transitions and data about their properties in the external magnetic fields enabled us to improve an existing theoretical approach developed previously in Ref. [35]. The obtained large volume of information about numerous quantum transitions in the $^4I_{13/2}$ and $^4I_{9/2}$ optical multiplets of Er^{3+} has been successfully interpreted in the framework of an improved theoretical approach by using only one set of basic parameters characterizing the crystal-field interaction, both magnetic dipole and electric quadrupole hyperfine interactions, and Zeeman interactions. As a result, we have matched all the above-mentioned absorption lines with particular hyperfine transitions.

We have also simulated the behavior of the ground-state hyperfine levels in low magnetic fields that shows nonlinear energy dependence accompanied by crossing or anticrossing points. The performed studies have demonstrated realistic possibilities to find specific experimental conditions (orientation and strength of the external magnetic field) when the frequency of the transition between two chosen hyperfine levels weakly depends on the value and orientation of the magnetic field, which can be useful in order to increase the optical QM coherence time. Finally, we note that the obtained results allow one to choose appropriate Λ schemes for the implementation of Raman QM protocols in a solid state. Herein, we have found 37 prospective Λ schemes with two ground hyperfine levels split by less than 1 GHz for the $^4I_{15/2} \rightarrow {}^4I_{9/2}$ transition at zero magnetic field. These observations promise rich opportunities for experimental implementations of the highly efficient Raman QM protocols on rare-earth ions in the isotopically purified $^{7}LiYF_4$ crystal.

ACKNOWLEDGMENTS

This work was financially supported by the Russian Science Foundation through the Grant No. 14-12-01333. The theoretical study of E.I.B. was also partially supported by the State subsidy in the area of scientific activities allocated to KFU, and by the President's stipend for young scientists. We thank S. L. Korableva and A. K. Naumov for growing the samples.

[1] W. Tittel, M. Afzelius, T. Chaneliére, R. Cone, S. Kröll, S. Moiseev, and M. Sellars, Laser Photonics Rev. **4**, 244 (2009).
[2] C. Simon, M. Afzelius, J. Appel, A. de la Giroday, S. J. Dewhurst, N. Gisin, C. Y. Hu, F. Jelezko, S. Kröll, J. H. Möller, J. Nunn, E. S. Polzik, J. G. Rarity, H. De Riedmatten, W. Rosenfeld, A. J. Shields, N. Sköld, R. M. Stevenson, R. Thew, I. A. Walmsley, M. C. Weber, H. Weinfurter, J. Wrachtrup, and R. J. Young, Eur. Phys. J. D **58**, 1 (2010).
[3] A. I. Lvovsky, B. C. Sanders, and W. Tittel, Nat. Photonics **3**, 706 (2009).
[4] M. P. Hedges, J. J. Longdell, Y. Li, and M. J. Sellars, Nature (London) **465**, 1052 (2010).
[5] M. Sabooni, Q. Li, S. Kröll, and L. Rippe, Phys. Rev. Lett. **110**, 133604 (2013).
[6] J. Phys. B: At. Mol. Opt. Phys. **45** (2012), special issue on quantum memory.
[7] *Focus on quantum memory*, special issue of New J. Phys. **17** (2015).
[8] B. Lauritzen, J. Minář, H. de Riedmatten, M. Afzelius, N. Sangouard, C. Simon, and N. Gisin, Phys. Rev. Lett. **104**, 080502 (2010).
[9] J. Dajczgewand, J.-L. Le Gouët, A. Louchet-Chauvet, and T. Chanelière, Opt. Lett. **39**, 2711 (2014).
[10] E. Saglamyurek, J. Jin, V. B. Verma, M. D. Shaw, F. Marsili, S. W. Nam, D. Oblak, and W. Tittel, Nat. Photonics **9**, 83 (2015).
[11] J. Dajczgewand, R. Ahlefeldt, T. Böttger, A. Louchet-Chauvet, J.-L. L. Gouët, and T. Chanelière, New J. Phys. **17**, 023031 (2015).
[12] F. R. Silva, A. Mirage, A. M. E. Santo, A. A. Martin, and S. L. Baldochi, J. Phys.: Conf. Ser. **249**, 12044 (2010).
[13] R. M. Macfarlane, R. S. Meltzer, and B. Z. Malkin, Phys. Rev. B **58**, 5692 (1998).
[14] M. N. Popova, Opt. Spectrosc. **119**, 544 (2015).
[15] R. M. Macfarlane, J. Lumin. **100**, 1 (2002).
[16] *Spectroscopic Properties of Rare Earths in Optical Materials*, edited by G. Liu and B. Jacquier, 1st ed., Springer Series in Materials Science Vol. 83 (Springer, Berlin, 2005).
[17] M. N. Popova, J. Rare Earths **32**, 230 (2014).
[18] C. W. Thiel, T. Böttger, and R. L. Cone, J. Lumin. **131**, 353 (2011).
[19] S. A. Moiseev and W. Tittel, New J. Phys. **13**, 063035 (2011).
[20] S. A. Moiseev, Phys. Rev. A **88**, 012304 (2013).
[21] E. S. Moiseev and S. A. Moiseev, New J. Phys. **15**, 105005 (2013).
[22] X. Zhang, A. Kalachev, and O. Kocharovskaya, Phys. Rev. A **90**, 052322 (2014).
[23] M. Hosseini, B. Sparkes, G. Campbell, P. Lam, and B. Buchler, Nat. Commun. **2**, 174 (2011).
[24] M. Zhong, M. P. Hedges, R. L. Ahlefeldt, J. G. Bartholomew, S. E. Beavan, S. M. Wittig, J. J. Longdell, and M. J. Sellars, Nature (London) **517**, 177 (2015).

[25] M. R. Brown, K. G. Roots, and W. A. Shand, J. Phys. C **2**, 593 (2002).
[26] N. Karayianis, J. Phys. Chem. Solids **32**, 2385 (1971).
[27] S. M. Kulpa, J. Phys. Chem. Solids **36**, 1317 (1975).
[28] H. P. Christensen, Phys. Rev. B **19**, 6564 (1979).
[29] G. M. Renfro, J. C. Windscheif, W. A. Sibley, and R. F. Belt, J. Lumin. **22**, 51 (1980).
[30] S. Hubert, D. Meichenin, B. Zhou, and F. Auzel, J. Lumin. **50**, 7 (1991).
[31] F. Auzel and Y. Chen, J. Lumin. **65**, 45 (1995).
[32] M. A. Couto dos Santos, E. Antic-Fidancev, J. Y. Gesland, J. C. Krupa, M. Lematre-Blaise, and P. Porcher, J. Alloys Compd. **275-277**, 435 (1998).
[33] J. P. Sattler and J. Nemarich, Phys. Rev. B **4**, 1 (1971).
[34] E. P. Chukalina, M. N. Popova, S. L. Korableva, and R. Abdulsabirov, Phys. Lett. A **269**, 348 (2000).
[35] M. N. Popova, E. P. Chukalina, B. Z. Malkin, and S. K. Saikin, Phys. Rev. B **61**, 7421 (2000).
[36] R. M. Macfarlane, A. Cassanho, and R. S. Meltzer, Phys. Rev. Lett. **69**, 542 (1992).
[37] R. Marino, I. Lorgeré, O. Guillot-Noël, H. Vezin, A. Toncelli, M. Tonelli, J.-L. Le Gouët, and P. Goldner, J. Lumin. **169**, 478 (2016).
[38] B. Z. Malkin, D. S. Pytalev, M. N. Popova, E. I. Baibekov, M. L. Falin, K. I. Gerasimov, and N. M. Khaidukov, Phys. Rev. B **86**, 134110 (2012).
[39] H. M. Grosswhite and H. Crosswhite, J. Opt. Soc. Am. B **1**, 246 (1984).
[40] V. V. Klekovkina, A. R. Zakirov, B. Z. Malkin, and L. A. Kasatkina, J. Phys.: Conf. Ser. **324**, 012036 (2011).
[41] L. A. Bumagina, V. I. Krotov, B. Z. Malkin, and A. K. Khasanov, Zh. Eksp. Teor. Fiz. **80**, 1543 (1981) [Sov. Phys. JETP **53**, 792 (1981)].
[42] W. T. Carnall, G. L. Goodman, K. Rajnak, and R. S. Rana, J. Chem. Phys. **90**, 3443 (1989).
[43] R. P. Gupta and S. K. Sen, Phys. Rev. A **7**, 850 (1973).
[44] A. Abragam and B. Bleaney, *Electron Paramagnetic Resonance of Transition Ions*, The International Series of Monographs on Physics (Oxford University Press, Oxford, U.K., 2012), p. 911.
[45] D. E. Castleberry and A. Linz, Appl. Opt. **14**, 2056 (1975).
[46] G. F. Koster, J. O. Dimmock, R. G. Wheeler, and H. Statz, *Properties of the Thirty-Two Point Groups* (MIT Press, Cambridge MA, 1963).
[47] See Supplemental Material at http://link.aps.org/supplemental/10.1103/PhysRevB.94.054429 for the tables of squared matrix elements of hyperfine transitions and tables of the transition frequencies.
[48] E. Fraval, M. J. Sellars, and J. J. Longdell, Phys. Rev. Lett. **92**, 077601 (2004).